Hydrodynamic Characteristics of Textured Microchannel Flow

Nastaran Rabiei
Department of Mechanical Engineering,
Northeastern University,
Boston, MA 02115
e-mail: rabiei.n@northeastern.edu

Carlos H. Hidrovo[1]
Department of Mechanical Engineering,
Northeastern University,
Boston, MA 02115
e-mail: hidrovo@northeastern.edu

Microchannel flow is of great interest across many disciplines and applications, from biochemical diagnostics to thermal management systems. Nonetheless, such flow requires large pumping power due to its small cross-sectional length scale. Textured surfaces have shown encouraging results in terms of drag reduction in external flows and at larger scales (turbulent regime). However, there have been some discrepancies in the literature regarding the possibility of drag/friction reduction in microscale internal flows (laminar regime), which is believed to be due to the absence of a proper definition for the reference baseline. The main goal of this paper is to determine whether the (rectangular) textures lead to drag/friction reduction while comparing their results with the correct reference. The rectangular trenches have been introduced on the side walls of the microchannels/microgaps to understand the underlying frictional physics by conducting numerical simulations and experiments. The effect of geometrical parameters of the rectangular trenches as well as the Reynolds number has been investigated on characteristics of the flow. A thorough analysis has been performed using a neural network (NN) to evaluate the potential drag reduction in textured microchannels. The results showed that using the correct reference baseline, no drag reduction was observed in textured microchannels with rectangular trenches. Moreover, the width-to-depth aspect ratio of the trenches and roughness (texture size to mean microchannel dimension) are introduced to be critical parameters in the flow behavior inside textured microchannels.

[DOI: 10.1115/1.4056783]

1 Introduction

Among the many methods that have been suggested to reduce drag in internal and external flows [1,2], using textured surfaces as a passive method has recently been one of the most interesting topics in fluid mechanics [3,4]. The interaction between the textures and the flowing fluid can reveal new aspects of hydrodynamic and thermal characteristics of the flow that can also result in transport augmentation [5–8]. The idea stems from nature, where the micro/nanoscale structures with their unique geometries on aquatic animals' skin, such as sharks, dolphins, and whales, can help them swim faster, experiencing 5–10% less resistance [9]. Flying birds also benefit from the drag reduction that is the result of the herringbone riblets on their feathers [10]. Due to the relatively high speed of these creatures, most of the drag reduction studies based on the bio-inspired structures lie in turbulent regime. Bio-inspired surfaces have many applications in the real world for energy-saving purposes, such as in aircraft [11–13], ships [14], high-speed trains, racing cars, wind turbine blades, gas/oil pipelines [15], and swimsuits [16,17].

The Utilization of textured surfaces has not been limited to large-scale applications, and they have also been tested in microscale systems with low Reynolds number applications for energy-saving purposes. Nowadays microchannels are the main components in microfluidic systems, and they are widely used in lab-on-a-chip devices, drug delivery systems [18], microelectronics cooling [19], and microgap evaporators [20,21]. Electro-osmotic flow of non-Newtonian fluids can be enhanced using textured surfaces to augment transport in micro/nanochannels that are used in biomedical diagnostic systems [22,23]. Due to the Darcy–Weisbach equation for laminar regime, the pressure drop is inversely proportional to the fourth power of the hydraulic diameter. Hence, the pumping power requirement gets significantly high for microchannel flow. Finding ways to decrease the pressure drop along the microchannel is always appreciated to improve the efficiency of a microfluidic system. At first sight, one may think that the textured surfaces increase the effective wetted surface area and more contact between the fluid and solid surface results in a shear stress (friction) increase. To get a better understanding of flow over textured surfaces in laminar regime, flow over a single cavity was studied [24]. Results showed that the key factor for drag behavior is the recirculation induced inside the cavity. The recirculation helps the liquid accelerate at the imaginary plane on top of the trench along the solid/liquid interface, lowering the skin drag and compensating for the increased wetted surface area. However, the skin drag is not the only concern in this case, and one should also be aware of the pressure drag. The pressure forces exerted on the front and back vertical walls of the cavity create a net force in the opposite direction of the flow, causing additional resistance. The tradeoff between the shear and pressure forces that are applied to the flow in the presence of textures will eventually determine the net drag experienced by the flow [25]. The Reynolds number of the flow, the geometry of the grooves, and their geometrical parameters, such as their depth, width, and spacing, directly affect this competition [26]. With the increase of the Reynolds number, the inertial forces (pressure drag) get stronger compared to the viscous forces (skin drag) revealing the negative effects of the recirculation [27]. The geometry of the textures is a prominent factor in characterizing the interaction between the fluid and solid surface. Different geometries for textures, such as rectangular, triangular, trapezoidal, curved (scalloped), and blades, have been tested for the purpose of drag reduction in external and internal flows. There has not been a precise clarification in the literature regarding which one of these geometries performs better in terms of laminar drag reduction. Generally, any geometry with sharp corners, i.e., rectangular, and triangular, causes the flow to experience unfavorable shear stress overshoots [24,28,29]. Spanwise grooves with trapezoidal, triangular, and scalloped geometries have shown lower pressure drop along the channel since they make the cross-sectional area variation very smooth compared to sudden changes with rectangular grooves. Moreover, since pressure forces are normal to their surface, their streamwise component on the groove walls with the three aforementioned geometries can be smaller [28,30]. Streamwise textures like the ones on butterfly wings, rice

---

[1] Corresponding author.

Contributed by the Fluids Engineering Division of ASME for publication in the Journal of Fluids Engineering. Manuscript received August 26, 2022; final manuscript received January 23, 2023; published online February 10, 2023. Assoc. Editor: Shahab Shojaei-Zadeh.

leaves, and fish scales have also been tested to reduce the pressure drop along the oil pipelines, and the first two have shown about 10% pressure drop reduction [31]. Introducing grooves within the grooves on surfaces, known as micronano scale nested-grooved surface, has been one of the other ideas that have shown drag reduction results by about 19% by reducing the negative effects of vortices and increasing the reverse shear stress [32].

Despite the many studies that have resulted in drag reduction using textured surfaces in small-scale and low Reynolds number flows [27,29,33,34], there have been some cases that prove otherwise [26,30,35]. The observations on laminar flow over converging-diverging (herringbone) riblets upstream of the curved backward-facing step have shown that the formation of a secondary flow by the riblets can help delay the flow separation. Although the pressure losses associated with the separation zone can be alleviated by these riblets, the flow losses caused by the interaction between the flow and riblets increase the pressure drop along the surface [36,37]. In a study, microchannels with curved (semicircular) textures have shown about 5% drag reduction in laminar regime [30], while in a different study, none of the cases that were tested with the exact geometry for textures, known as fan-shaped ribs, have resulted in total drag reduction [26]. Moreover, there have been contradictory results regarding the possibility of drag reduction for streamwise textured surfaces [30,38,39]. The source of this ambiguity can be attributed to the lack of defining a correct reference baseline to perform valid comparisons. In recent literature, using the definition of energy dissipation, the valid baseline is defined as the smooth microchannel to maintain the same occupying mass or volume of the fluid as the textured channel [30].

In this paper, the main goal is to first revisit the study of spanwise rectangular trenches and their effect on the hydrodynamic characteristics of the flow by considering a correct reference baseline in the calculations. The Poiseuille number from the Darcy–Weisbach equation has been calculated for all the cases to do the comparison. The pressure drop used in the calculation of the Poiseuille number considers both the pressure and frictional resistive forces against the flow and hence is a good resource to evaluate the flow losses. The important geometrical parameters of the trenches are considered in their nondimensional form to study their effect individually. The effect of the Reynolds number in a fully laminar regime has also been considered. After determining the flow behavior in the presence of these spanwise rectangular trenches inside microchannels/microgaps in different Reynolds numbers, a more comprehensive approach has been adopted to investigate the combined effect of all the geometrical parameters on the total Poiseuille number using a neural network (NN) framework to identify any potential drag reduction.

2 Problem Setup and Methodology

2.1 Numerical Framework. The computational domain and boundary conditions for two-dimensional and three-dimensional simulations are depicted in Fig. 1. The trenches are perpendicular to the direction of the fluid flow (spanwise). The fluid enters the domain from the left boundary with uniform velocity as the inlet boundary condition. The value of the velocity at the inlet is calculated based on the desired volumetric flowrate divided by the cross-sectional area at the inlet $\left(U_{\text{inlet}} = \frac{Q}{A_{\text{inlet}}}\right)$. Zero-gage pressure has been used as the boundary condition at the outlet assuming the fact that the fluid is discharged into the atmosphere. Due to the geometrical and hydrodynamic symmetry in the centerline, half of the full microchannel has been considered for the simulations meaning that the velocity gradient at the centerline is zero. There is also a no-slip boundary condition on the walls. Since there are no heating sources considered in this study, the thermophysical property variations of the working fluid (water) have also been neglected. All the thermophysical properties of water have been considered at 20 °C in this study ($\rho_f = 998.21\,\frac{\text{kg}}{\text{m}^3}$, $\mu_f = 0.0010017\,\text{Pa}\cdot\text{s}$). The finite element scheme in COMSOL MULTIPHYSICS 5.5 has been used for discretizing the continuity and momentum Eqs. (1) and (2) to solve for the fluid velocity ($\boldsymbol{u}$) and pressure field (P). Since low Reynolds numbers are tested in this study, the simulations are performed in steady-state and laminar regime. Second-order discretization has been used for all the simulations, and the relative tolerance is set to be 0.0001

$$\text{Continuity:}\ \nabla.\boldsymbol{u} = 0 \tag{1}$$

$$\text{Momentum:}\ \nabla(\rho_f\,\boldsymbol{u}.\boldsymbol{u}) = -\nabla P + \nabla\cdot\left[\mu_f\left(\nabla\boldsymbol{u} + (\nabla\boldsymbol{u})^T\right)\right] \tag{2}$$

The geometrical parameters of the rectangular textures are labeled as a for spacing between the trenches, b for width of the trench, c for depth of the trenches, and w_p for the microchannel width in the land region. The width of the land region (w_p) is calculated such that the textured microchannel maintains the same volume as the equivalent baseline with width W (Eq. (3)). The definition of an equivalent baseline is necessary to obtain the proper characteristic lengths (D_h and A_{avg}) for a textured microchannel for valid comparisons [30]. These parameters are used in the Reynolds number and the Poiseuille number calculations as can be seen in Eqs. (4) and (5).

To characterize the hydrodynamic behavior of the microchannel flow, the Poiseuille number has been calculated and compared for all the cases. From the Darcy–Weisbach equation for fully developed laminar flow, the Poiseuille number is a quantifiable value of the hydraulic resistance along a channel. For a microchannel flow with a length of L, a hydraulic diameter of D_h, and a cross-sectional area of A_{avg}, the Poiseuille number can be calculated using Eq. (5). Mathematically, the Poiseuille number can be defined as the slope of the pressure drop versus flowrate in a channel. Larger values for the slope of this linear relation indicate high hydraulic resistance, and hence high required pumping power to overcome this resistance. In this equation, ΔP is the pressure drop along the channel, Q is the volumetric flowrate, and μ is the dynamic viscosity of the fluid. The pressure drop is calculated from the pressure difference between any two cross sections along the channel. The volumetric flowrate and length of all the cases that have been tested at a specific Reynolds number are the same. In two-dimensional analysis, the average cross-sectional area (A_{avg}) and the hydraulic diameter (D_h) of different textured microchannels are the same since they maintain the same volume. Therefore, having all the parameters constant between different cases and neglecting the less than 1% variation in the fluid properties, the Poiseuille number comparison simply stands for the pressure drop comparison between any two cases. However, in three-dimensional analysis, the hydraulic diameter of different cases is not necessarily the same despite maintaining the same volume. This leads to introducing a different parameter to compare the hydraulic resistance between different 3D cases, such as $\frac{\text{Po}}{{D_h}^2}$ although it is not a nondimensional parameter. Since the focus of this study is mainly on the two-dimensional analysis, the Poiseuille number has been used for comparison purposes, and the use of $\frac{Po}{{D_h}^2}$ for three-dimensional cases needs further investigation which is beyond the goal of this study

$$WL = w_pL + (2cb);\ L = n(a+b) \tag{3}$$

$$\text{Re} = \frac{\rho U_{\text{avg}} D_h}{\mu};\quad U_{\text{avg}} = \frac{Q}{A_{\text{avg}}} \tag{4}$$

$$\text{Po} = \frac{2\,\Delta P\,A_{\text{avg}}\,D_h^2}{\mu\,Q\,L} \tag{5}$$

A single period of a textured microchannel can be divided into two parts: the land region and the trench region. To clearly show how each one of these sections affects the Poiseuille number

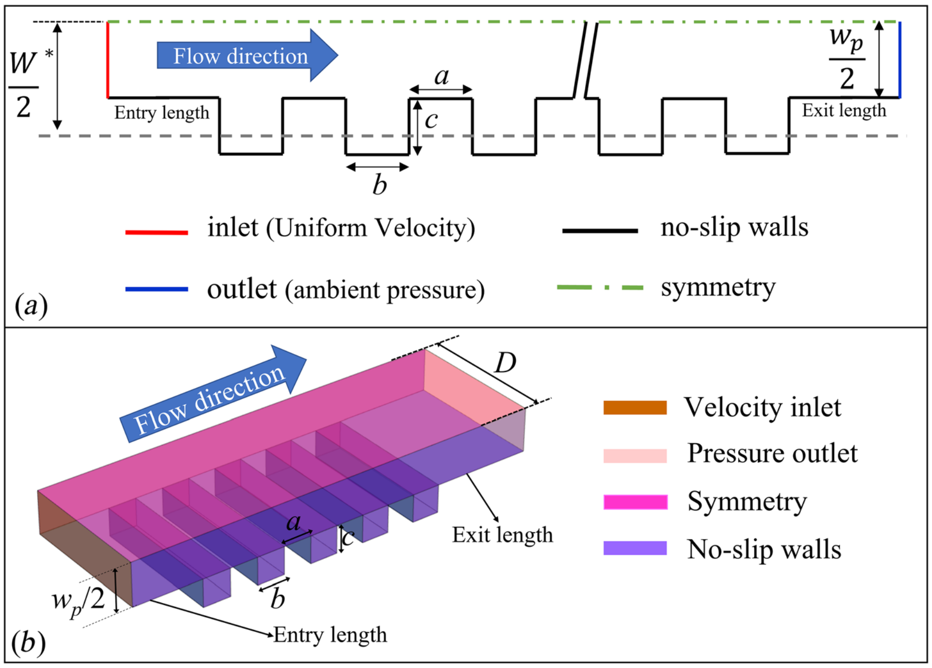

Fig. 1 Computational domain and boundary conditions for (*a*) 2D and (*b*) 3D simulations of spanwise rectangular trenches. The geometrical parameters of the trenches are labeled as *a*, *b*, *c*, and w_p, which correspond to the spacing between the trenches, the width of the trench, depth of the trench, and width of the land region, respectively (*The gray dashed line shows the equivalent baseline with respect to the textured microchannel and it is only for illustration purposes in this figure and does not appear in the computational domain).

behavior in a textured channel, nondimensional geometrical parameters have been introduced. Parameter a/c defined as the "land aspect ratio" considers the effects of the land region. Parameter b/c defined as the "trench aspect ratio" is defined to study the effects of the trench region, and parameter c/W defined as the "roughness" considers the confinement effects. The c/W values considered in this study are 0.05, 0.2, 0.4, and 0.6. The range of the a/c and b/c values also lies between 0 and 50. The Reynolds numbers used in this study are 5, 200, and 1000. The reference baseline for the two-dimensional simulations is flowed between two parallel plates that are 100 μm apart from each other with the Poiseuille number 96. For three-dimensional simulations, the reference baseline is flowed inside a channel with a 100 μm by 100 μm square cross section with the Poiseuille number value 56. These reference Poiseuille number values are used to make comparisons between the textured and smooth baseline.

2.2 Model Validation

2.2.1 Hydrodynamic Fully Developed Condition. The fully developed state of the flow is a concept that should be considered in the textured cases tested in this study since the Darcy–Weisbach equation and therefore the derived equation for the Poiseuille number, Eq. (5), are valid when the laminar internal flow has reached hydrodynamic fully developed condition. However, due to a periodic variation in the cross-sectional area of the textured microchannel reaching a locally fully developed condition is almost impossible for the flow, unless the length that fluid travels before the next variation of the cross-sectional area is long enough depending on the Reynolds number. Figure 2 depicts the centerline velocity of a textured microchannel at Reynolds number 200 with rectangular trenches in which a and c are 20 μm and b is 60 μm. To maintain the mass balance, the centerline velocity increases at cross-sectional contraction and decreases at cross-sectional expansion, and this pattern repeats itself as the periodic geometrical variation. A closer look at this periodic centerline velocity at the very beginning of the textured region shows that the variation of the minimum and maximum values of the velocity from one period to another cannot be neglected (much more than 1% variation). As the flow moves forward the repeating pattern of the centerline velocity becomes more consistent with less than 1% variation between the peaks and valleys of the adjacent periods. Based on this observation, the hydrodynamic *globally fully developed condition* can be defined as textured microchannels in which the flow does not experience a locally fully developed condition but can reach this state of consistent periodic variation of the velocity field. Since all the Poiseuille number calculations in this study have been performed over the region where flow has reached the hydrodynamic globally fully developed condition, the entry and exit length do not have any effects on the results.

2.2.2 Mesh Resolution Study. Mesh resolution studies have been conducted on textured microchannel computational domains as well as the smooth baseline. Structured (mapped) mesh has been used for all the cases. The elements are finer near the no-slip walls and sharp corners to capture the boundary layer effects near the walls. Table 1 shows a step-by-step refinement of elements and evaluation of the Poiseuille number that has led to the final choice of the element size where the error is less than 1%. The theoretical value of the Poiseuille number for flow between two smooth parallel plates (96) has been used as the benchmark for mesh resolution study of the smooth baseline. Based on the error percentages for the smooth baseline and applying the same grids to the textured microchannels and considering their difference percentage, grid "M2" with an average two-dimensional element size in the x-direction as small as 0.000125 L ($\sim$0.5 μm) and in the y-direction as small as 0.002 W ($\sim$0.2 μm), is used to perform all the simulations. As an example, the mesh resolution study results for two of the textured cases have also been included in Table 1 with their difference percentage of the Poiseuille number calculation compared to the former grid. The 0.168% error for the smooth baseline simulation with the "M2" grid indicates the numerical accuracy of the method used in this study. The mesh resolution studies for the three-dimensional simulations also

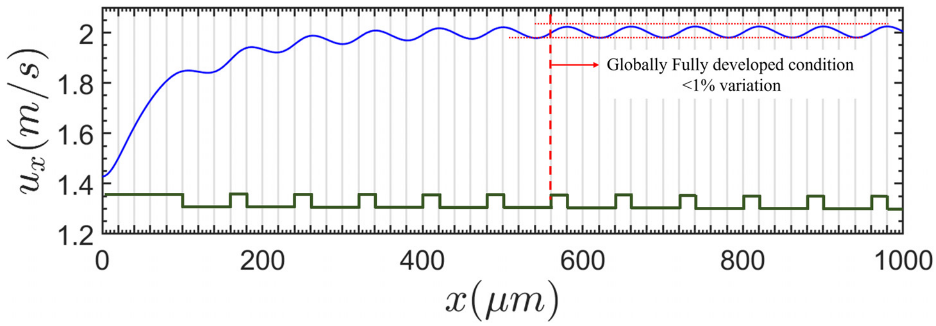

Fig. 2 **Centerline velocity of a textured microchannel with $a = c = 20\,\mu$m and $b = 60\,\mu$m. The flow reaches globally fully development at $x = 580\,\mu$m, where the periodic variation of the centerline velocity gets less than 1%.**

Table 1 **Mesh resolution study in two-dimensional analysis for smooth baseline with $W = 100\,\mu$m and textured microchannels with $a/c = 1$, $b/c = 0.25$, $c/W = 0.2$, and $a/c = 1$, $b/c = 39$, $c/W = 0.2$**

	Baseline			$a/c = 1$, $b/c = 0.25$, $c/W = 0.2$			$a/c = 1$, $b/c = 39$, $c/W = 0.2$		
	Element no.	*Po*	Error %	Element no.	*Po*	Difference %	Element no.	*Po*	Difference %
M1	210,000	94.824	1.225	209,200	122.290	0.989	208,200	114.892	0.904
M2	1,705,200	95.838	0.168	1,139,930	122.628	0.027	1,138,005	115.346	0.034
M3	3,360,000	95.965	0.036	3,478,200	122.649	0.002	3,407,580	115.377	0.001

The nondimensional parameters represent the land aspect ratio, trench aspect ratio, and roughness, respectively.

resulted in the same sizes as the two-dimensional elements in the x- and y-directions as well as 0.005 times the depth ($\sim$0.5 μm) in the z-direction, which shows about 0.25% error in the Poiseuille number value of flow inside a smooth channel with square cross section.

2.2.3 Experimental Validation. Experimentation has been performed on a couple of textured microchannels to assure the validity of the numerical simulations which will eventually be used to conduct optimization studies on the effect of geometrical parameters on the Poiseuille number. The replicating molds for the polydimethylsiloxane (PDMS) microchannel layouts are created through the photolithographic procedure. The overall schematic of the experimental setup is shown in Fig. 3(*a*). Four parameters, including liquid flowrate, microchannel pressure drop, water temperature, and channel dimensions are measured to obtain the relation between the flowrate and the pressure drop in microchannels. The results of each channel are then compared with the results of the numerical simulations and the theoretical baseline. The liquid flowrate is calculated by measuring the amount of accumulated water in the microchannel outlet over a specific time using a high-precision mass scale (A and D mass balance). In addition, Sensirion flow meters help keep track of the flowrate variation over time. Two Omega differential pressure transducers with ranges of 0–1 psid and 0-5 psid are used to measure the pressure difference between the pressure taps designed at the beginning and end of the textured area of the microchannel that is depicted in Fig. 3(*b*). The pressure difference between the two ends of the differential pressure transducer deflects the pressure-sensitive diaphragm, which is converted into an electrical signal, usually voltage. The calibration then helps correspond the voltage values to the actual pressure that is being measured by the device. Therefore, in all the experiments of this study, the accuracy of the pressure drop measurements along the microchannels is assured by meticulously calibrating the pressure transducers. A K-type Omega thermocouple is also used to measure the temperature of water at the exit to obtain the thermophysical properties of water for the Poiseuille number calculation based on Eq. (5). Since the cross-sectional area and the hydraulic diameter of the tested microchannels are also needed for the Poiseuille number calculation, cross-sectional and top view images are taken by a charged-coupled device camera that is connected to an upright Nikon microscope with objectives of 20X, NA = 0.4, and 40X, NA = 0.65. The PDMS replica of the microchannel is cut into thin slices along the microchannel and placed on the side so that cross-sectional images can be taken directly. It is very important to cut the slices as straight as possible to avoid any errors associated with image processing of the tilted cross sections. The images are then processed by a MATLAB image processing code to measure the cross-sectional area and perimeter. The code detects the edges of the cross section and counts the number of pixels inside the confined area to measure the cross-sectional area. The perimeter is also measured by counting the number of pixels detected at the edges and multiplying them by the real pixel sizes of the camera. The local hydraulic diameter can then be calculated based on $D_h = \frac{4A}{P}$.

Figure 4 depicts the results for five different cases and the smooth baseline that was tested to do the validation. The error bars include the precision errors from multiple readings and uncertainty of the measurement devices. The experiments have been performed at both states of increasing and decreasing the flowrate (Q) to account for the hysteresis effects of the sensors. The Poiseuille number obtained for the 100 μm × 100 μm baseline microchannel at different Reynolds numbers shows a good agreement with the theory with a maximum error of about 7% that guarantees the accuracy of the measurement methods and experimental setup. The results of the textured microchannels also show extremely good agreement with the results from the three-dimensional numerical simulations, which assures the assumptions made in the numerical simulations are close to the real-world experiments and are valid.

3 Results and Discussions

3.1 Control Volume Analysis and Poiseuille Number Definition. The definition of the Poiseuille number can be rewritten based on the contributing resistive forces against the flow that result in pressure drop along a specific length of the channel. Figure 5 shows two different control volumes on a textured microchannel, one with the inlet and outlet positioned in the land region (land-to-land) and the other in the textured region (trench-to-trench). The momentum equation in the x-direction (Eq. (6)) indicates that the pressure drop between the inlet and outlet of the control volume is proportional to the ratio of the resistive forces and the effective cross-sectional area that the inlet and outlet pressures are acting on. Several analyses on different cases have proven that the shear force and the pressure drop values are independent of the location of the control volume with the same length along the microchannel. However, the resistive pressure force acting on the vertical walls of the trench due to the induced recirculation varies as the location of the control volume changes. Based on the momentum balance, this is due to the change in the effective cross-sectional area that the inlet and outlet pressures are acting on. To eliminate the dependence of the results on the selection of the control volume, the average cross-sectional area has been considered in the momentum balance, which is equal for all the cases tested in this study (100 μm). Further analysis has shown that the pressure force calculated from the momentum balance is the weighted average of the different pressure forces in control volumes (a) and (b) in Fig. 5. A proper selection of the transversal characteristic length helps remove the contradictions that can happen between the Poiseuille number and total resistive force behavior when defining different control volumes and assure a valid evaluation. Reliance on only the land-to-land or the trench-to-trench control volume analysis in Poiseuille number/total force calculations can result in misinterpretations resulting in false friction reduction/increase statement that has happened in the previous studies [24,26]. Therefore, this explains clearly why we have been maintaining the same volume between all the cases so that we can use a global cross-sectional area and hydraulic diameter in calculations to eliminate any ambiguity

$$\Delta P\, A_{\text{avg}} = F_s + F_p, \quad \text{where } F_p = \frac{(F_{p,A} \times a) + (F_{p,B} \times b)}{a+b} \tag{6}$$

Equation (7) defines the total Poiseuille number based on the resistive forces: pressure and shear force. In other words, by separating these two components the total Poiseuille number can be considered as the sum of shear and pressure Poiseuille numbers. The subscript s refers to the shear component and the subscript p refers to the pressure component. The behavior of the individual Poiseuille numbers can provide helpful information to understand the total Poiseuille number behavior with respect to the geometrical parameters of the textured microchannel and the Reynolds number

$$\mathrm{Po}_{\text{total}} = \frac{2\,\Delta P\, A_{\text{avg}}\, D_h^2}{\mu\, Q\, L} = \frac{\Delta P\, A_{\text{avg}}}{\dfrac{QL\mu}{2D_h^2}} = \frac{\Sigma F_s + \Sigma F_p}{\dfrac{QL\mu}{2D_h^2}} = \frac{\Sigma F_s}{\dfrac{QL\mu}{2D_h^2}} + \frac{\Sigma F_p}{\dfrac{QL\mu}{2D_h^2}} = \mathrm{Po}_s + \mathrm{Po}_p \tag{7}$$

3.2 Effect of Geometrical Parameters

3.2.1 Effect of Land Aspect Ratio (a/c). Figure 6 depicts the shear, pressure, and total Poiseuille number with respect to the land aspect ratio (a/c) for different values of roughness (c/W) at Reynolds number 5 when the trench aspect ratio (b/c) is equal to unity. According to Fig. 6(a), two different behaviors can be observed for the shear Poiseuille number (Po_s) with respect to a/c depending on the c/W values. For the cases where c/W is relatively

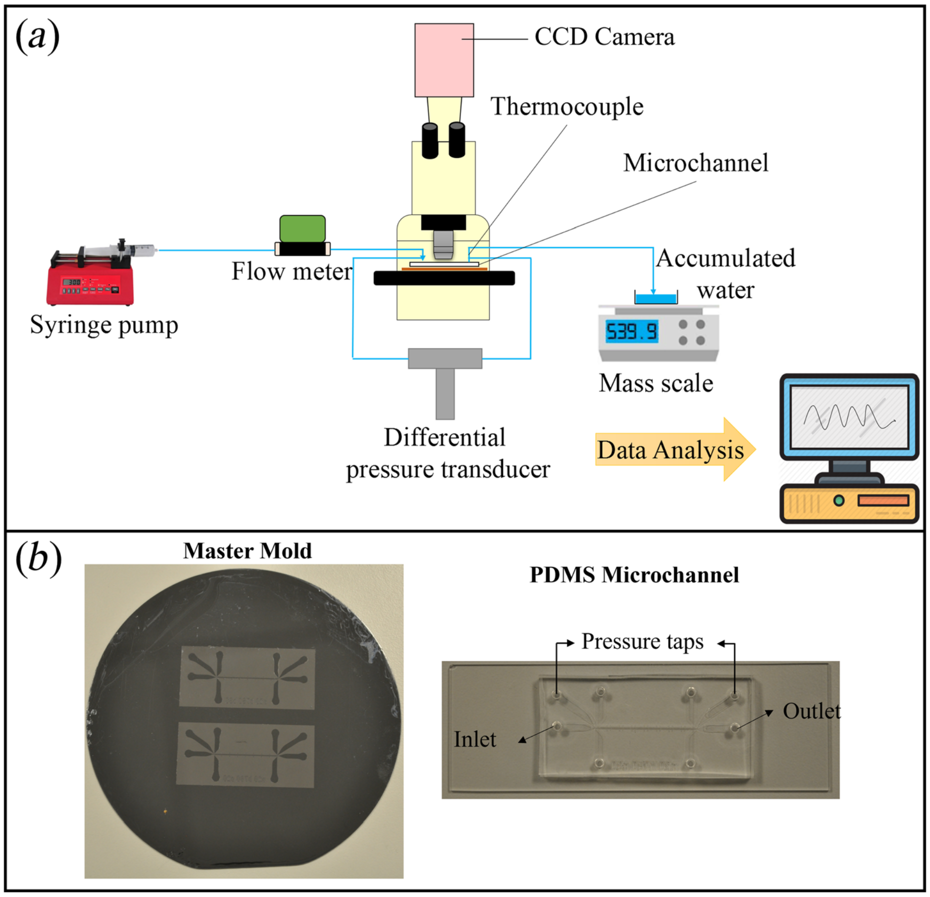

Fig. 3 (*a*) Schematic diagram of the experimental setup for pressure-flow measurements of the baseline and textured microchannels. (*b*) The master mold was fabricated using the photolithography method and the PDMS microchannel was bonded to the glass slide using the Plasma cleaner.

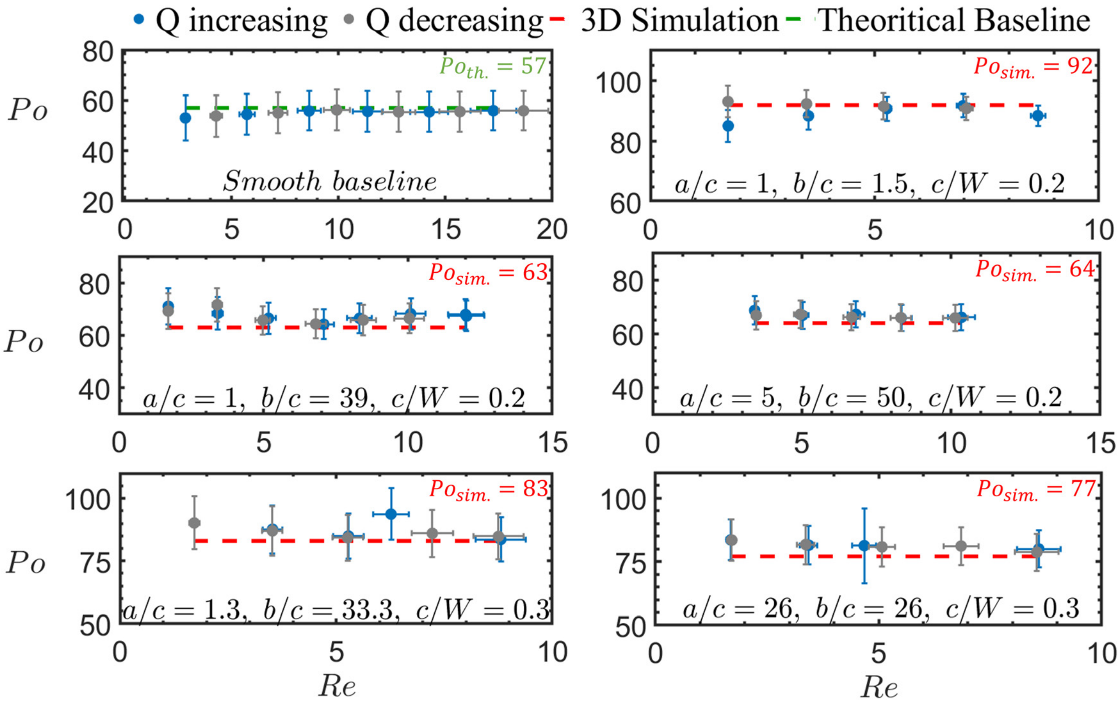

Fig. 4 Experimental validation results for the smooth baseline and five textured microchannels. The agreement between the experiment and theory for the smooth baseline is indicative of the accuracy of the experimental setup and measurement methods. The agreement between the experiment and three-dimensional simulation results assures the validity of the assumptions in the numerical analysis used in this work.

small, 0.05 and 0.2, with the increase of the a/c value, the shear Poiseuille number increases; however, for the cases with relatively large c/W values, 0.4 and 0.6, the shear Poiseuille number has a descending trend. Eventually, the shear Poiseuille number for all the c/W values asymptotes to the smooth baseline value ($Po_{\text{baseline}} = 96$) when a/c gets larger than ten. In general, as the land aspect ratio (a/c) gets smaller, the spacing between the trenches gets narrower and they get closer to each other. Therefore, the main flow stream experiences less interaction with the solid surface in the land region and more overall slippage along

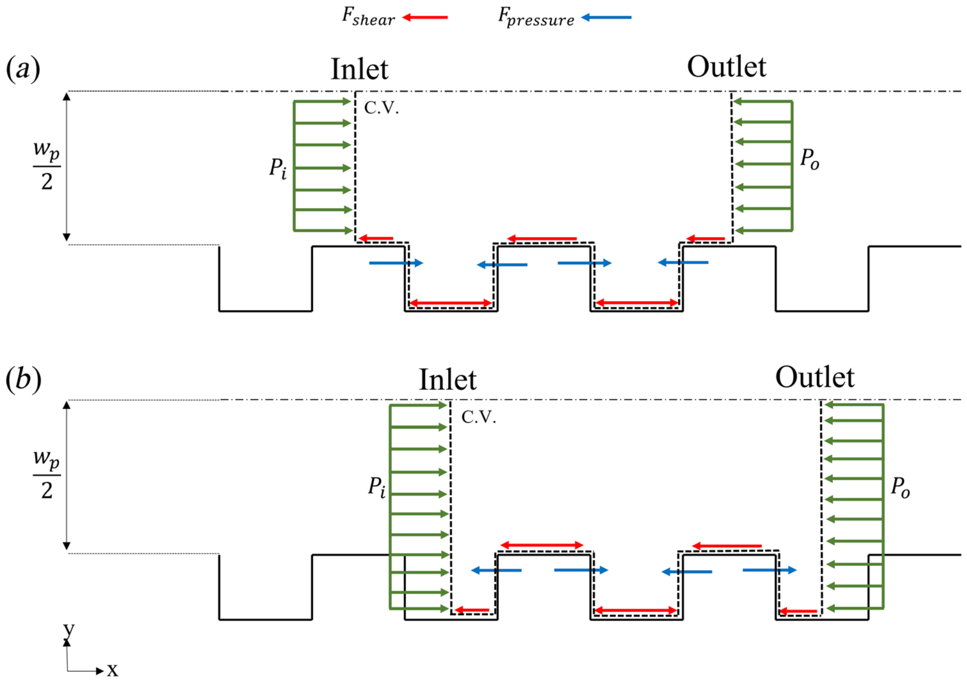

Fig. 5 Two different approaches for control volume analysis on a textured microchannel: (*a*) inlet and outlet positioned in the land region (land-to-land control volume) and (*b*) inlet and outlet positioned in the textured region (trench-to-trench control volume). The effective forces are the shear forces on the horizontal surfaces, pressure forces on the vertical surfaces of the trenches, and inlet and outlet cross-sectional areas.

the channel. This can be noticed by looking at the shear Poiseuille numbers in Fig. 6(*a*) for the cases with c/W values of 0.05 and 0.2 with $a/c < 24$ and $a/c < 3$, respectively, where more than 2% shear Poiseuille number reduction occurs compared to the smooth baseline.

Although the same logic applies for larger roughness values (c/W) regarding a lower percentage of interface between the main flow stream and the solid surface in the land region when a/c value is small, there must be a second contributing factor that outweighs this effect and leads to a different behavior. This can be attributed to the emergence of the confinement effect as the roughness value (c/W) increases. Generally, as the c/W value increases, the width of the land region (w_p), which plays an important role in confinement of the textured microchannels, gets smaller. The mathematical relation between the geometrical parameters of the rectangular trenches for maintaining the same occupying volume in Eq. (3) also shows that when the roughness value (c/W) and the trench aspect ratio (b/c) are constant, the width of the land region (w_p) gets smaller as the land aspect ratio value (a/c) decreases. Therefore, for larger values of c/W, 0.4 and 0.6, when a/c value is extremely small, the width of the land region (w_p) gets small enough to activate the dominance of confinement effect over the slippage caused by less liquid–solid interaction which leads to high velocity gradients and high frictional forces. As the a/c value increases for the same roughness (c/W) values, the land region gets wider (larger w_p) and the confinement effect gradually subsides while the shear Poiseuille number asymptotes to the smooth baseline value. The confinement effects can also explain larger values of the shear Poiseuille number for larger c/W values.

The pressure Poiseuille number (Po_p) behavior depicted in Fig. 6(*b*) shows a descending trend with respect to the land aspect ratio (a/c) for all the roughness (c/W) values. As mentioned before, at a specific c/W value, the width of the land region (w_p) increases with the increase of a/c value. The main flow stream is less disturbed by the presence of the trenches/recirculation as the width of the land region (w_p) gets wider, and the pressure forces exerted on the vertical walls of the trench will have a smaller contribution in the total resistive forces of the control volume analysis (Fig. 5) compared to the pressure forces at the inlet and outlet of the control volume. Hence, as the spacing between the trenches gets wider (larger a/c), the pressure Poiseuille number decreases until it reaches zero when there are no trenches in the microchannel (smooth baseline). Like the shear Poiseuille number behavior with respect to a/c, the pressure Poiseuille number value increases as c/W increases. Since the trench aspect ratio (b/c) for all the cases plotted in Fig. 6 is equal to unity, the streamline patterns inside the trench are alike; however, the size of the recirculation is not. As c/W increases, the size of the trench as well as the recirculation gets larger and results in higher pressure forces on the vertical walls, and therefore higher pressure Poiseuille number.

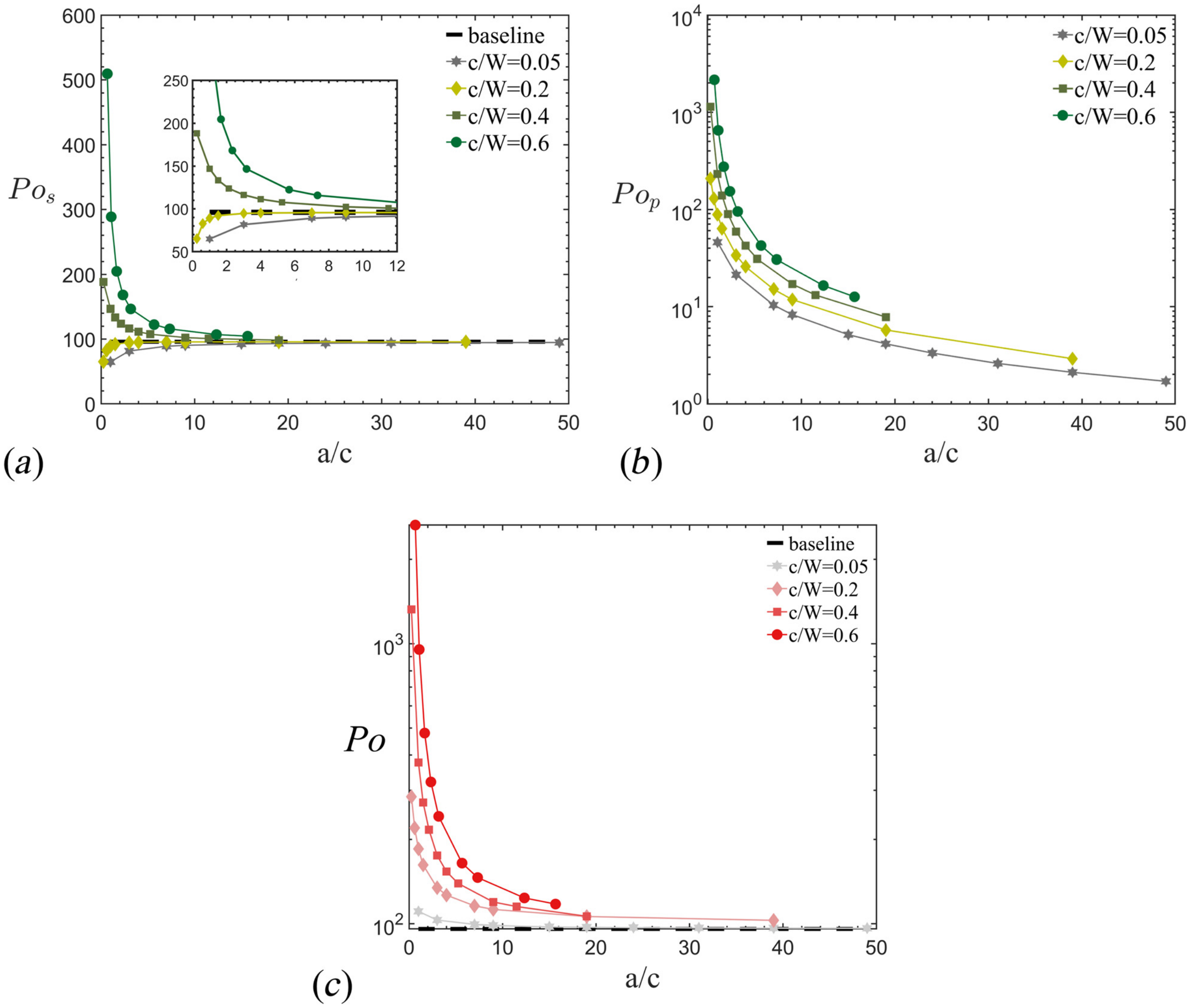

Fig. 6 (*a*) Shear (Po_s), (*b*) pressure (Po_p), and (*c*) total Poiseuille number (Po) with respect to the land aspect ratio (a/c) for different roughness (c/W) values and the trench aspect ratio (b/c) of 1 at Reynolds number 5

Figure 6(*c*), the plot for the total Poiseuille number (Po) with respect to the land aspect ratio (a/c), shows that no matter what the value of the roughness (c/W) is, the total Poiseuille number of a textured microchannel with spanwise rectangular trenches reduces with the increase of a/c and asymptotes to the Poiseuille number of a smooth baseline. Moreover, the pressure Poiseuille number (Po_p) values in Fig. 6(*b*) are one order of magnitude larger than the shear Poiseuille number (Po_s) values. This fact can then be used to justify the behavior of the total Poiseuille number with respect to the land aspect ratio (a/c) when the trench aspect ratio (b/c) is constant, which is dominated by the pressure component (Po_p).

3.2.2 Effect of Trench Aspect Ratio (b/c). To study the effect of the trench aspect ratio (b/c) on the behavior of the total Poiseuille number and its components, similar plots have been depicted in Fig. 7 for the textured microchannels with different values of roughness (c/W) and a/c value of unity at Reynolds number 5. According to Fig. 7(*a*), the shear Poiseuille number (Po_s) behavior with respect to b/c depends on the value of c/W. For the cases with c/W values of 0.05 and 0.2, the shear Poiseuille number decreases initially with the increase of b/c until it reaches a minimum value at a specific b/c. With further increase of b/c, the shear Poiseuille number increases and asymptotes to that of the smooth baseline value. Conversely, for larger c/W values, 0.4 and 0.6, the behavior of the shear Poiseuille number is the opposite. This is like what was observed with the behavior of the shear Poiseuille number with respect to a/c for different c/W values discussed in Sec. 3.2.1, Fig. 6(*a*). To better understand the flow and Poiseuille number behavior, Fig. 8 illustrates the streamline patterns of flow inside the trenches for all the roughness values (c/W) at Reynolds number 5. The recirculation inside the trench is induced by the pressure difference between the back and front vertical walls. For a specific value of c/W in Fig. 8, as b/c increases, meaning that the trench gets wider, the recirculation inside the trench becomes more vulnerable to collapse. At some point, the main flow streamlines bend inside the trench and due to more liquid–solid interaction at the bottom of the trench, the frictional forces that had vanished because of the recirculation will emerge once again. In this study, the trench width-to-depth aspect ratio at which the recirculation is fully collapsed, and the main flow stream finds its way all the way down to the bottom of the trench is labeled as the critical trench aspect ratio or CTAR. From Fig. 8, the CTAR value for the cases with roughness values (c/W) values of 0.05, 0.2, 0.4, and 0.6 at Reynolds number 5 are, respectively, equal to 2.8, 2.7, 1.8, and 1.7. The following then explains the behavior of the shear Poiseuille number with respect to the trench aspect ratio (b/c) for roughness values (c/W) of 0.05 and 0.2. As b/c increases before reaching the CTAR, the size of the recirculation inside the trench gets larger meaning that the percentage of the liquid–solid interface decreases in the land region of the microchannel and therefore the main flow stream experiences less frictional resistance. This trend continues until b/c value is equal to the CTAR where the recirculation is not strong enough to resist the penetration of the main flow stream inside the trench and the recirculation collapses.

The Peclet number (Pe) is defined as the ratio of diffusion time over advection time. Considering momentum diffusion into the depth of the trench c and momentum advection along the width of the trench b, the definition of the Peclet number can be rewritten as in Eq. (8), where u_t is the mean streamwise velocity at the top of the trench and ν is the kinematic viscosity of the fluid. Plotting the Peclet number at the top of the trench for all the roughness values (c/W) at Reynolds number 5 in Fig. 9 provides a different approach on understanding the underlying physics behind the collapse of the recirculation inside the trench as the trench aspect ratio (b/c) gets larger. According to Fig. 9, for a specific c/W value, the Peclet number increases with the increase of b/c until it reaches a maximum value and then drops with the further increase of b/c value. The maximum value of the Peclet number happens at a b/c value right before the CTAR at that specific c/W value. As the Peclet number increases before b/c reach its maximum value, it means that with the recirculation getting larger in size, the momentum advection in the direction of the flow becomes more dominant over the momentum diffusion into the depth of the trench. At the maximum point where the recirculation is at its strongest state, the momentum advection reaches its strongest level compared to the momentum diffusion. With further increase of b/c value, the main flow stream gradually diffuses more inside the trench (recirculation collapse) rather than for advection to happen along the width of the trench, which means that the main flow stream is always seeking a route with less resistance

$$\mathrm{Pe}_{xy} = \frac{t_{\text{diffusion}}}{t_{\text{advection}}} = \frac{\dfrac{c^2}{\nu}}{\dfrac{b}{u_t}} = \frac{c^2 u_t}{b\,\nu} \tag{8}$$

According to Fig. (8), the streamline patterns, collapse of the recirculation at the CTAR, and flow behavior for the large roughness (c/W) values, 0.4 and 0.6, as the trench aspect ratio (b/c) value increases, are the same as that of the cases with smaller c/W values, 0.05 and 0.2. However as stated before, the behavior of the shear Poiseuille number for large c/W values, 0.4 and 0.6, is quite different from the smaller c/W values with respect to b/c. For instance, for the cases with c/W value of 0.4, the shear Poiseuille number first increases with the increase of b/c and reaches its maximum value at a b/c value which is not necessarily equal to the CTAR. For b/c values larger than that of the extremum point, the shear Poiseuille number drops. The difference in the behavior of the shear Poiseuille number for cases with large and small c/W values is related to the confinement effects that were discussed in Sec. 3.2.1 to explain the shear Poiseuille number behavior for large c/W values with respect to the variation of a/c. It is known that for large c/W values, the width of the land region (w_p) gets narrower compared to the cases with smaller c/W values. According to Eq. (3), when the roughness value (c/W) and the land aspect ratio (a/c) are constant, the width of the land region (w_p) gets smaller as the trench aspect ratio value (b/c) increases. For large c/W values, 0.4 and 0.6, as b/c increases, the width of the land region (w_p) is narrow enough to make the confinement effect dominant over the shear-free recirculation inside the trench. Therefore, as the b/c value increases, the confinement effect becomes more prominent leading to an increase in the velocity gradient, shear stress, and shear Poiseuille number. The ascending trend in the shear Poiseuille number does not last forever and at a specific trench aspect ratio (b/c) that is larger than the CTAR, it starts a descending trend. Although for b/c values larger than the CTAR the recirculation collapses and there is more liquid–solid interface at the bottom of the trench, the flow experiences a drop in the shear Poiseuille number which can be related to the main flow stream experiencing more expansion of the cross-sectional area on average at larger values of b/c. This can therefore alleviate the increase in the shear Poiseuille number due to the confinement effect for larger b/c values, and result in a slight decrease in the shear Poiseuille number.

Moreover, as can be noticed from Fig. 7, the cases with c/W values of 0.6 have been tested in a smaller range of trench aspect ratio (b/c) value. This is because the data points for the cases with c/W of 0.6 are limited due to the geometrical restriction of maintaining the same volume for all the cases. For b/c values larger than 3, textured microchannels are not geometrically feasible when the roughness value (c/W) is 0.6. The shear Poiseuille number for c/W value of 0.6 has an ascending behavior with the increase of b/c in the range that it is tested, which is due to the dominance of the confinement effect at this roughness value that was similarly explained for the cases with c/W value of 0.4.

As plotted in Fig. 7(*b*), the behavior of the pressure Poiseuille number (Po_p) with respect to the trench aspect ratio (b/c) for all the roughness (c/W) values is alike. The pressure Poiseuille

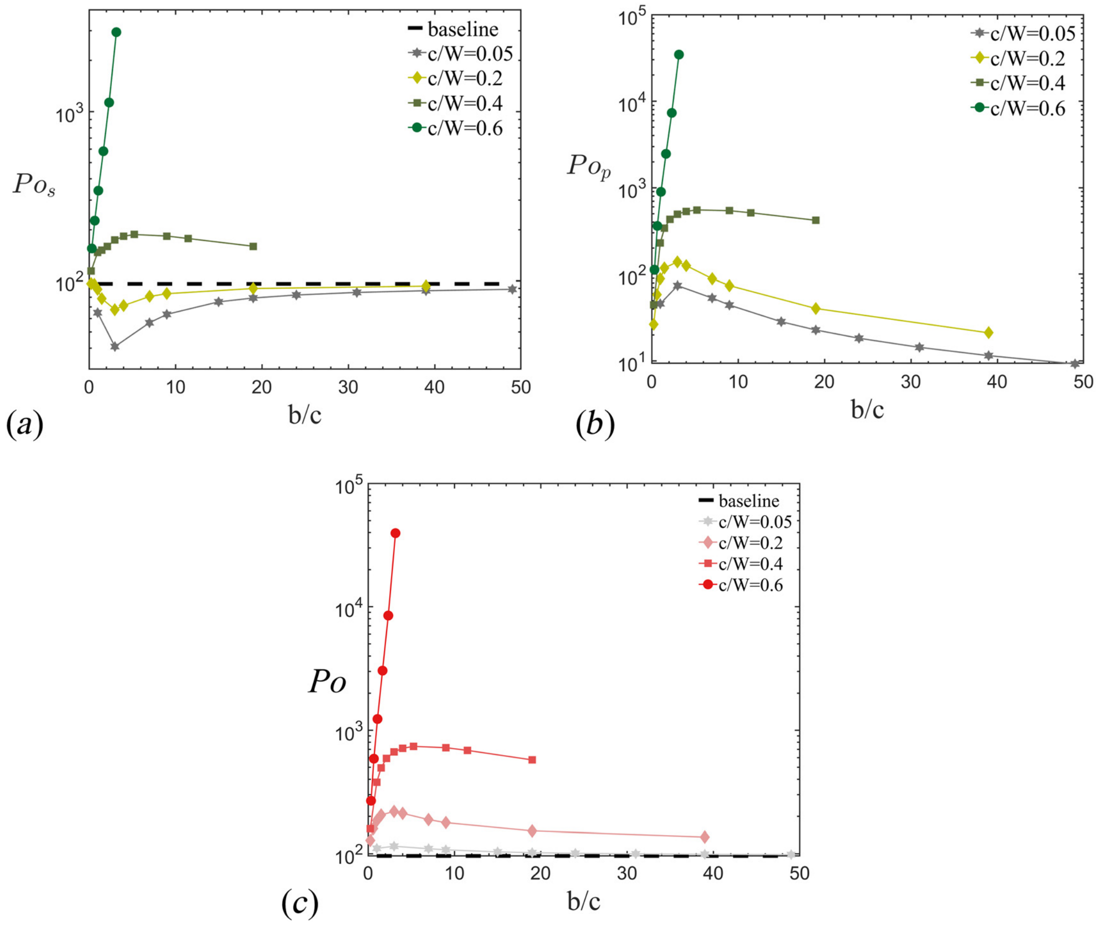

Fig. 7 (*a*) Shear (Po_s), (*b*) pressure (Po_p), and (*c*) total Poiseuille number (*Po*) with respect to the trench aspect ratio (*b/c*) for different roughness (*c/W*) values and the land aspect ratio (*a/c*) of 1 at Reynolds number 5

number has larger values for the cases with large c/W because the trenches get deeper and the pressure forces on the vertical walls exert on a larger area that results in larger pressure Poiseuille number values. In addition, with the increase of b/c, the pressure Poiseuille number initially increases until adopting a maximum value at a specific b/c and then decreases. In general, the increase in b/c the recirculation induced inside the trench gets larger and stronger which can result in larger pressure forces on the vertical walls of the trench. This prominence continues to the point where the recirculation is in one piece, right when b/c equals the CTAR. For b/c values larger than the CTAR, the pressure forces affecting the vertical walls of the trench become less prominent since the recirculation has collapsed and is not as strong as before. Looking at the streamline patterns in Fig. 8 and comparing them with the pressure Poiseuille number behavior in Fig. 7(*b*), this explanation is only valid for the cases with c/W values of 0.05 and 0.2. For the cases with larger c/W values, the maximum value of the pressure Poiseuille number does not occur at the CTAR, and instead at a b/c value larger than the CTAR. The reason for this delay can be explained by the dominance of the confinement effect. When the c/W value is large, the width of the land region (w_p) is narrow, and it gets narrower as the b/c value increases. Hence, the main flow stream is more affected by the recirculation inside the trench. Even after the recirculation collapse, the portion that is left on the left corner of the trench still has negative pressure effects on the main flow stream. This then results in lingering adverse pressure effects for b/c values larger than the CTAR. From Fig. 7(*c*), the behavior of the total Poiseuille number (*Po*) is the same as the pressure Poiseuille number which shows the dominance of the pressure Poiseuille number (Po_p) over the shear Poiseuille number (Po_s) in defining the total Poiseuille number behavior. With further increase of b/c value, the total Poiseuille number only gets closer to the value of a smooth baseline and never goes below.

3.3 Effect of the Reynolds Number. Figure 10 depicts the total Poiseuille number (*Po*) behavior with respect to the land aspect ratio (a/c) for different roughness (c/W) values and the Reynolds numbers when the trench aspect ratio (b/c) is equal to unity. The results show that the total Poiseuille number for any c/W value independent from the Reynolds number asymptotically approaches the Poiseuille number value of the smooth baseline and never goes below that value. Based on the calculations, the variation of the total Poiseuille number with respect to the Reynolds number is less than 2% for c/W values of 0.05 and 0.2. This small percentage of variation can be attributed to computational error and is negligible. However, for larger c/W values, 0.4 and 0.6, the variation of the total Poiseuille number with respect to Reynolds number is more than 5% when the a/c value is smaller than 3. This is because for larger c/W values the recirculation inside the trench plays a more prominent role and becomes more susceptible to higher inertial effects induced by higher Reynolds numbers. For the c/W value of 0.4, when the Reynolds number increases from 5 to 200 the jump is about 19% maximum for an a/c value of 0.25, and for the Reynolds number increasing from 200 to 1000, the jump is about 9% maximum for the same value of a/c. For the c/W value of 0.6, the maximum total Poiseuille number jump is 63% for a/c value of 0.333 when increasing the Reynolds number from 5 to 200, and 26% for the same a/c value when increasing the Reynolds number from 200 to 1000. Note

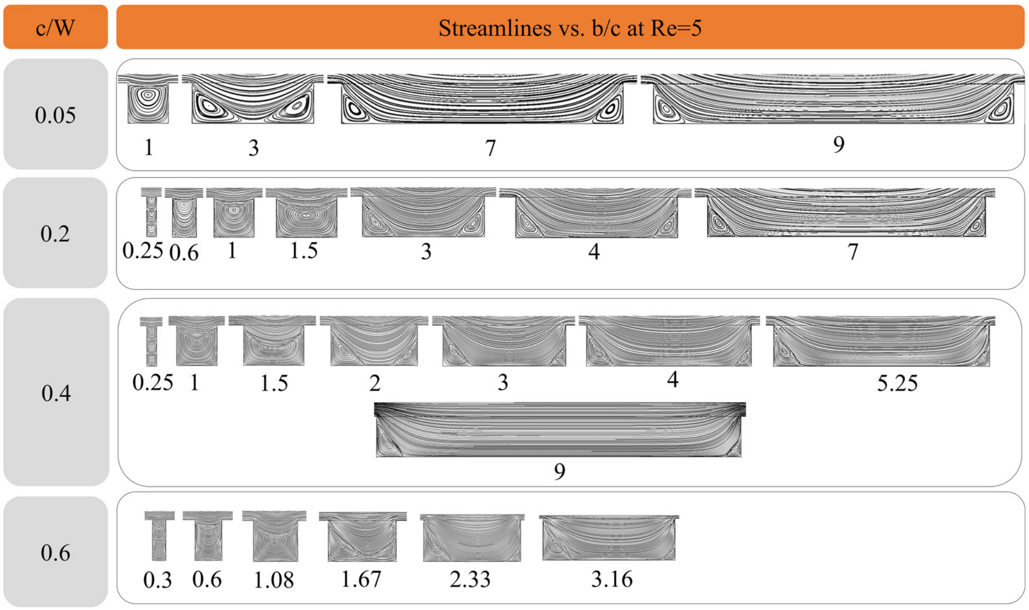

Fig. 8 Streamline patterns inside the trench with respect to the trench aspect ratio (*b/c*) at the roughness (*c/W*) values of 0.05, 0.2, 0.4, and 0.6 at Reynolds number 5

that these relatively large variations with respect to the Reynolds number variation may not be noticeable in the plots of Fig. 10 for large *c*/*W* values since the total Poiseuille number varies in a wider range with respect to the land aspect ratio (*a*/*c*) compared to the smaller roughness (*c*/*W*) values.

To better understand the effect of Reynolds number on the total Poiseuille number behavior and its components when only the trench aspect ratio (*b*/*c*) changes and the land aspect ratio (*a*/*c*) is constant, the streamline patterns for the cases with a *c*/*W* value of 0.2 at three different Reynolds numbers are illustrated in Fig. 11. The CTAR at which the recirculation inside the trench has fully collapsed is significantly affected by the Reynolds number. The CTAR values for the Reynolds numbers 5, 200, and 1000 are, respectively, 2.7, 4.7, and 12.1 for the cases where their roughness value (*c*/*W*) is 0.2 and their land aspect ratio (*a*/*c*) is 1. Moreover, as the Reynolds number increases, momentum advection will be dominant over momentum diffusion inside the trenches leading to less deflection of the main flow stream. After the recirculation disruption at high Reynolds numbers, the recirculation that is induced on the left bottom corner of the trench gets larger. These observations can help explain the behavior of the pressure Poiseuille number (Po_p) depicted in Fig. 12 with respect to the Reynolds number while the roughness (*c*/*W*) and the trench aspect ratio (*b*/*c*) are variable, and the land aspect ratio (*a*/*c*) is equal to 1. Since the recirculation collapse is delayed at high Reynolds numbers at a specific *c*/*W* value, and even after its breakage the portion of the recirculation left inside the trench is large, the negative pressure forces affecting the vertical walls of the trench also become prominent leading to larger pressure Poiseuille number value for higher Reynolds numbers at the same *b*/*c* value.

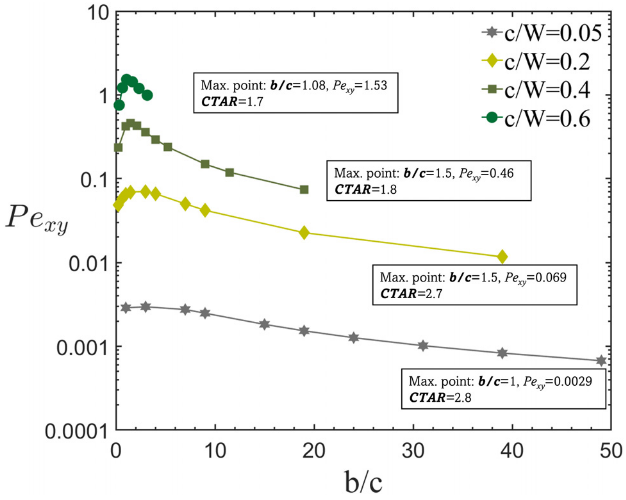

Fig. 9 The Peclet number (Pe_{xy}) calculated at the top of the trench for different cases with respect to their trench aspect ratio (*b/c*) values for different values of roughness (*c/W*), 0.05, 0.2, 0.4, and 0.6, and the land aspect ratio (*a/c*) of 1 at Reynolds number 5. Information regarding the maximum point and the CTAR value is also included in the graph for each roughness (*c/W*) value.

Similarly, Fig. 13 depicts the shear Poiseuille number (Po_s) with respect to the trench aspect ratio (*b*/c) for different roughness values (*c*/*W*) and Reynolds numbers. The behavior of the shear Poiseuille number with Reynolds number is dependent on the *c*/*W* value. For small *c*/*W* values, 0.05 and 0.2, at a specific *b*/c value, the shear Poiseuille number decreases as the Reynolds number increases. While for larger *c*/*W* values, 0.4 and 0.6, the shear Poiseuille number mostly increases with the increase of the Reynolds number for a specific range of the *b*/*c* value. Generally, the larger the recirculation gets at the bottom left corner of the trench with the increase of the Reynolds number, the liquid–solid interaction decreases in the land region, and the main flow stream experience less frictional forces at higher Reynolds numbers. For instance, for the two *b*/*c* values of 9 and 19 when the *c*/*W* value is 0.2, the shear Poiseuille number even reaches negative values at Reynolds number 1000, meaning that the frictional forces are in favor of the main flow stream. This can explain the behavior of the shear Poiseuille number with respect to the Reynolds number for the cases with small *c*/W values, 0.05 and 0.2. For the cases with larger *c*/*W* values, 0.4 and 0.6, this explanation is only valid for large *b*/*c* values where the intactness of the recirculation inside the trench at higher Reynolds number overweighs the shear increasing factors and resulting in less shear Poiseuille number as the Reynolds number increases. For instance, at *c*/*W* value of 0.4, the shear Poiseuille number at Reynolds number 200 gets smaller than at Reynolds number 5 when the *b*/*c* value is larger than two.

Figure 14 shows the total Poiseuille number (*Po*) behavior with respect to the trench aspect ratio (*b*/*c*) for different values of

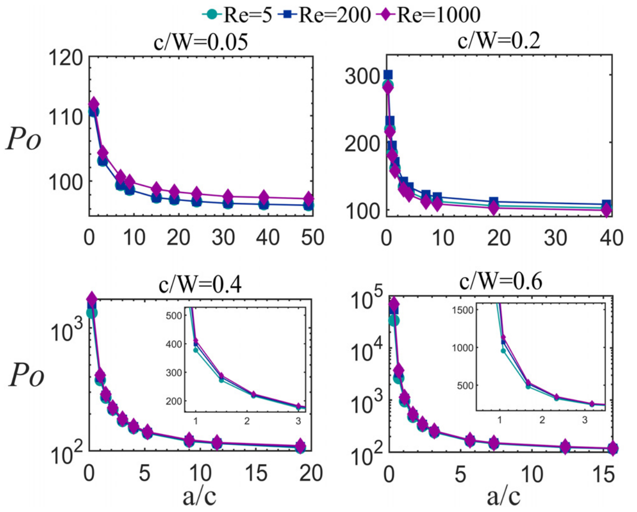

Fig. 10 Total Poiseuille number (*Po*) with respect to the land aspect ratio (*a/c*) for roughness (*c/W*) values of 0.05, 0.2, 0.4, and 0.6 at three Reynolds numbers of 5, 200, and 1000 when the trench aspect ratio (*b/c*) is 1

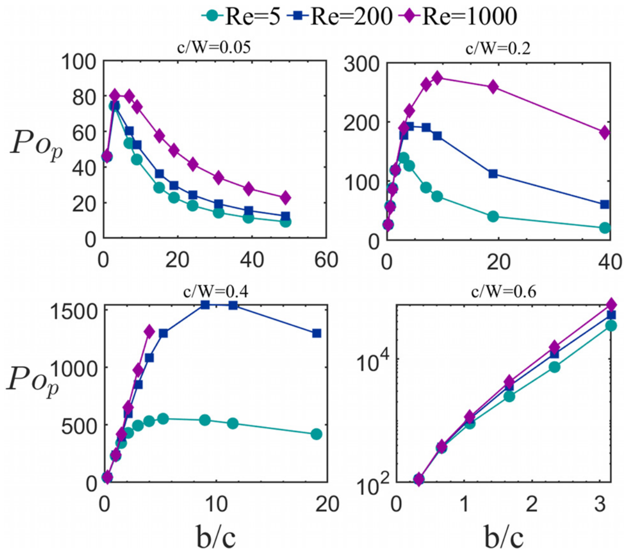

Fig. 12 Pressure Poiseuille number (Po_p) with respect to the trench aspect ratio (*b/c*) for the roughness (*c/W*) values of 0.05, 0.2, 0.4, and 0.6 at Reynolds numbers of 5, 200, and 1000 when the land aspect ratio (*a/c*) is 1

roughness (*c*/*W*) when the land aspect ratio (*a*/*c*) is constant. Based on this figure, the total Poiseuille number increases for the same *b*/*c* value as the Reynolds number increases. Since the total Poiseuille number variation with respect to *b*/*c* is dominated by the pressure forces, the same trend applies when it comes to the effect of the Reynolds number. The CTAR for the cases with roughness (*c*/*W*) value of 0.05 is 2.8, 3.0, and 3.2 at Reynolds number 5, 200, and 1000, respectively. While the CTAR for the cases with *c*/*W* value of 0.2 is 2.7, 4.7, and 12.1 at Reynolds numbers of 5, 200, and 1000, respectively. For the cases with *c*/*W* values of 0.4, the CTAR are 1.8 and 11.8 at Reynolds numbers of 5 and 200. These numbers for the CTAR for different roughness and Reynolds number values show that as the *c*/*W* increases the increase of the CTAR value gets more sensitive to the Reynolds number variation. This is because the inertial effects due to the increase of Reynolds number become more prominent as the confinement effects at higher roughness values increase. It should also be noted that no matter what the Reynolds number is, no total Poiseuille number reduction has been detected compared to the smooth baseline for the examined cases.

3.4 Combined Effect of the Geometrical Parameters. A three-dimensional plot of the behavior of the total Poiseuille number (*Po*) with respect to all the nondimensional parameters: trench aspect ratio (*b*/*c*), land aspect ratio (*a*/*c*), and roughness (*c*/*W*) at Reynolds number 5 has been depicted in Fig. 15 by training a NN on the data at hand. This is necessary to get a better understanding of the combined effect of the geometrical parameters on the Poiseuille number behavior. Among the machine learning methods, NN is used in this study to create a continuous map for the

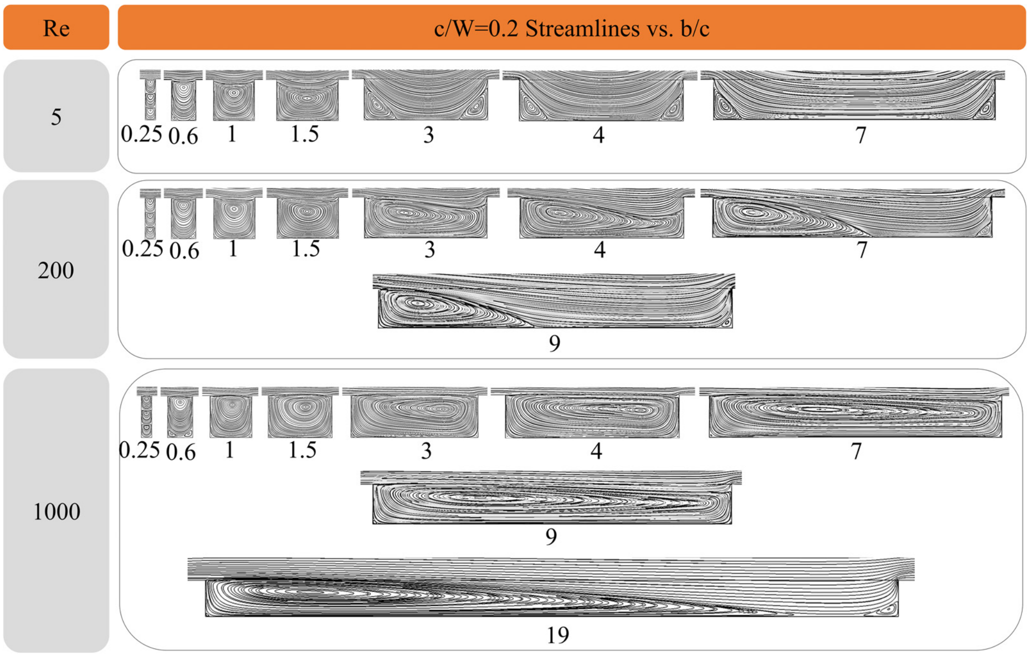

Fig. 11 Streamline patterns inside the trench for with respect to the trench aspect ratio (*b/c*) for the cases with the roughness (*c/W*) value of 0.2 at three Reynolds numbers of 5, 200, and 1000

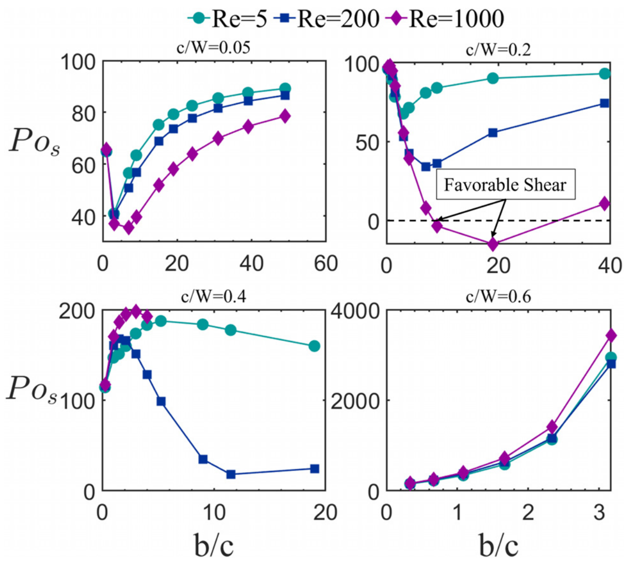

Fig. 13 Shear Poiseuille number (Po_s) with respect to the trench aspect ratio (*b/c*) for the roughness (*c/W*) values of 0.05, 0.2, 0.4, and 0.6 at Reynolds numbers of 5, 200, and 1000 when the land aspect ratio (*a/c*) is 1

Poiseuille number behavior with respect to the three contributing geometrical parameters: *b*/*c*, *a*/*c*, and *c*/*W*. This method is the most suitable approach for this study due to its accurate and fast performance to deal with complex systems.

Neural network is an interconnected group of nodes formed generally in multiple layers that could learn to build a computational structured framework and relate training data to the desired output data through an evolving mapping function. Each layer of NN consists of several neurons that translate inputs to outputs through mathematical functions. In this study, a feed-forward back-propagation NN is built using the TENSORFLOW package in Python. An extensive study is performed to tune the hyperparameters of the NN before generating any results. For example, the architecture of the NN is tuned to achieve the best accuracy while avoiding overfitting, which leads to a NN with two layers and 16 neurons in each layer. The loss function is defined as the discrepancy between the actual value and the prediction from the NN which is optimized using a combination of Adams optimizer and limited-memory Broyden-Fletcher-Goldfarb-Shanno (LBFG-S) method together with Xavier's initialization method, while the hyperbolic tangent function is employed as the activation function. 15,000 data is generated based on the dimensionless geometrical parameters, *a*/*c*, *b*/*c*, and *c*/*W*, to feed the NN and achieve a total loss value of 1×10^{-6}.

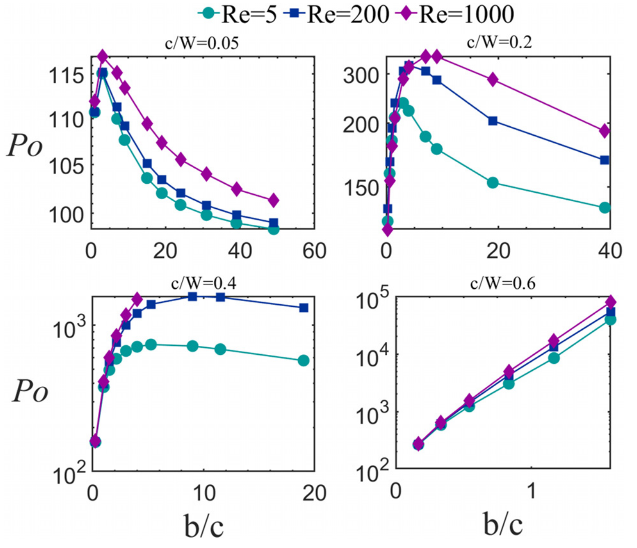

Fig. 14 Total Poiseuille number (*Po*) with respect to the trench aspect ratio (*b/c*) for the roughness (*c/W*) values of 0.05, 0.2, 0.4, and 0.6 at Reynolds numbers of 5, 200, and 1000 when the land aspect ratio (*a/c*) is 1

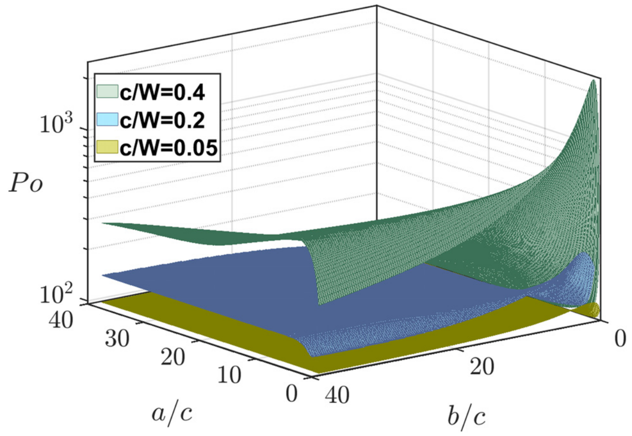

Fig. 15 Total Poiseuille number (*Po*) with respect to the land aspect ratio (*a/c*) and the trench aspect ratio (*b/c*) for the roughness (*c/W*) values of 0.05, 0.2, and 0.4 generated using neural networks training

The general behavior of the Poiseuille number is the same for all the roughness values and for larger roughness (*c*/*W*) values, the value of the total Poiseuille number increases. For all *c*/*W* values the total Poiseuille number experiences its maximum value when the *a*/*c* value is very small and *b*/*c* value is relatively small. At Reynolds number 5, the maximum Poiseuille number for *c*/*W* value of 0.05 is 124.4 which occurs at $a/c = 0.1$ and $b/c = 1.3$. For *c*/*W* value of 0.2, the maximum Poiseuille number is 248.1 which occurs at $a/c = 0.1$ and $b/c = 2.1$. For *c*/*W* value of 0.4 the maximum Poiseuille number is 2510 which occurs at $a/c = 0.1$ and $b/c = 0.9$. The corresponding *b*/*c* values for the maximum Poiseuille number at all *c*/*W* values are very close to the CTAR where the negative pressure effects are at their maximum strength. Moreover, as *a*/*c* gets smaller, the width of the land region (w_p) also gets smaller leading to more prominent confinement effects. These two contributing factors can justify the occurrence of a peak for the total Poiseuille number at small values of *a*/*c* and *b*/*c*. On the other hand, the minimum value of the total Poiseuille number happens when *a*/*c* value is large and *b*/*c* value is small, meaning narrower trenches that are far distant from each other resembling a smooth baseline. Therefore, the minimum value does not go below the smooth baseline value. The minimum value of the total Poiseuille number for *c*/*W* values of 0.05, 0.2, and 0.4 are 96.04, 96.01, and 97.3 happen at *a*/*c* value of 34.9, 14.4, and 20.5, and *b*/*c* value of 0.1, 0.2, and 0.1, respectively. The resemblance of the textured microchannels to the smooth baseline is also true when *b*/*c* value gets very large. As can be seen for all *a*/*c* values, as *b*/*c* increases, the 3D surface reaches a plateau that gets closer to the value of the Poiseuille number for a smooth baseline ($Po_{\text{baseline}} = 96$).

4 Conclusion

In this paper, the attempts are to resolve the mystery surrounding the feasibility of drag/friction reduction in microchannels/microgaps by employing textured surfaces, specifically rectangular spanwise textures. The smooth reference baseline has been considered to maintain the same occupying volume as the textured microchannels to make valid comparisons. The nondimensional geometrical parameters of the trenches including the land and trench aspect ratios and roughness have been introduced for a more generalized assessment. The effect of these geometrical parameters and Reynolds number is then investigated using numerical simulations. In general, the recirculation induced inside the trench can be beneficial for the shear Poiseuille number reduction; however, the negative pressure effects are not in favor of the total Poiseuille number. In other words, there are a few cases in that microtexturing helps reduce the shear Poiseuille number, but the adverse pressure forces induced by the recirculation outweigh the decrease in the shear Poiseuille number and result in an increase in the total Poiseuille number. Although the results based on the trained neural network did not show any drag reduction, they provided a comprehensive understanding of the behavior of the total Poiseuille number with respect to the nondimensional geometrical parameters of the rectangular trenches altogether. Based on those results, flow experiences a higher resistance as the roughness value is large and both land and trench aspect ratios are relatively small, meaning small trench width and spacing between the trenches. As the land and trench aspect ratios increase at any roughness value, the total Poiseuille number asymptotes to a constant value of the smooth baseline at the extremes. Understanding the flow behavior in textured microchannels can help design efficient microfluidics systems in different applications, such as drug delivery and microelectronics cooling. For instance, by knowing the underlying physics, the regular roughness/microtextures in the inner surfaces of the microtubes/channels can be engineered such that specific supply pressure is created to deliver the drug to an organ in the body.

Acknowledgment

The authors wish to thank Massimo DiMuzio and Grace McDonough for their help with the experiments and simulations.

Funding Data

- National Science Foundation (NSF) (Grant No. CBET-1705958; Funder ID: 10.13039/100000001).

Data Availability Statement

The datasets generated and supporting the findings of this article are obtainable from the corresponding author upon reasonable request.

Nomenclature

a = spacing between the trenches
A_{avg} = average cross-sectional area
b = width of the trench
c = depth of the trench
D_h = hydraulic diameter
F_p = resistive pressure force
F_s = resistive shear force
L = total length of the microchannel
n = number of trench-land periods along the microchannel
P = fluid pressure
Po = Poiseuille number
Po_p = pressure Poiseuille number
Po_s = shear Poiseuille number
Q = volumetric flow rate
Re = Reynolds number
U, u = streamwise flow velocity
W = width of the equivalent baseline
w_p = microchannel width in the land region
ΔP = pressure drop
μ_f = fluid dynamic viscosity
ρ_f = fluid density

References

[1] Abdulbari, H. A., Yunus, R. M., Abdurahman, N. H., and Charles, A., 2013, "Going Against the Flow-A Review of Non-Additive Means of Drag Reduction," J. Ind. Eng. Chem., **19**(1), pp. 27–36.

[2] Mahmoudabadbozchelou, M., Rabiei, N., and Bazargan, M., 2018, "Numerical and Experimental Investigation of the Optimization of Vehicle Speed and Inter-Vehicle Distance in an Automated Highway Car Platoon to Minimize Fuel Consumption," SAE Intl. J CAV, **1**(1), pp. 3–12.

[3] Kant, K., and Pitchumani, R., 2021, "Laminar Drag Reduction in Microchannels With Liquid Infused Textured Surfaces," Chem. Eng. Sci., **230**, p. 116196.

[4] Chitsaz, N., Siddiqui, K., Marian, R., and Chahl, J. S., 2021, "Numerical and Experimental Analysis of 3D Micro-Corrugated Wing in Gliding Flight," ASME J. Fluids Eng., **144**(1), p. 011205.

[5] Kandlikar, S. G., 2008, "Exploring Roughness Effect on Laminar Internal Flow–Are We Ready for Change?," Nanoscale Microscale Thermophys. Eng., **12**(1), pp. 61–82.

[6] Chai, L., Xia, G. D., and Wang, H. S., 2016, "Parametric Study on Thermal and Hydraulic Characteristics of Laminar Flow in Microchannel Heat Sink With Fan-Shaped Ribs on Sidewalls – Part 1: Heat Transfer," Int. J. Heat Mass Transfer, **97**, pp. 1069–1080.

[7] Lee, C., and Kim, C.-J., 2011, "Underwater Restoration and Retention of Gases on Superhydrophobic Surfaces for Drag Reduction," Phys. Rev. Lett., **106**(1), p. 14502.

[8] Li, P., Campbell, M., Zhang, N., and Eckels, S. J., 2022, "Investigation of Relationship Between Flow Structures and Drag Forces on Microfin Enhanced Surfaces Using Large Eddy Simulations," ASME J. Fluids Eng., **144**(10), pp. 1–12.

[9] Bhushan, B., 2009, "Biomimetics: Lessons From Nature - An Overview," Philos. Trans. R. Soc. A Math. Phys. Eng. Sci., **367**(1893), pp. 1445–1486.

[10] Chen, H., Rao, F., Shang, X., Zhang, D., and Hagiwara, I., 2013, "Biomimetic Drag Reduction Study on Herringbone Riblets of Bird Feather," J. Bionic Eng., **10**(3), pp. 341–349.

[11] Viswanath, P. R., 2002, "Aircraft Viscous Drag Reduction Using Riblets," Prog. Aerosp. Sci., **38**(6–7), pp. 571–600.

[12] Bechert, D. W., and Hage, W., 2006, "Drag Reduction With Riblets in Nature and Engineering," *Flow Phenomena in Nature: Inspiration, Learning and Applications*, Vol. 2, WIT Press, Southampton, UK, pp. 457–469.

[13] Büttner, C. C., and Schulz, U., 2011, "Shark Skin Inspired Riblet Structures as Aerodynamically Optimized High Temperature Coatings for Blades of Aeroengines," Smart Mater. Struct., **20**(9), p. 094016.

[14] Stenzel, V., Wilke, Y., and Hage, W., 2011, "Drag-Reducing Paints for the Reduction of Fuel Consumption in Aviation and Shipping," Prog. Org. Coat., **70**(4), pp. 224–229.

[15] Luo, Y., and Zhang, D., 2012, "Experimental Research on Biomimetic Drag-Reducing Surface Application in Natural Gas Pipelines," Oil Gas Eur. Mag., **38**(4), pp. 213–214.

[16] Stefani, R., 2012, "Olympic Swimming Gold: The Suit or the Swimmer in the Suit?," Significance, **9**(2), pp. 13–17.

[17] Luo, Y., Yuan, L., Li, J., and Wang, J., 2015, "Boundary Layer Drag Reduction Research Hypotheses Derived From Bio-Inspired Surface and Recent Advanced Applications," Micron, **79**, pp. 59–73.

[18] Liu, D., Zhang, H., Fontana, F., Hirvonen, J. T., and Santos, H. A., 2017, "Microfluidic-Assisted Fabrication of Carriers for Controlled Drug Delivery," Lab Chip, **17**(11), pp. 1856–1883.

[19] Hidrovo, C., and Kenneth, G., 2008, "Active Microfluidic Cooling of Integrated Circuits," *Electrical, Optical and Thermal Interconnections for 3D Integrated Systems*, Artech, Boston, MA, pp. 293–330.

[20] Ahmed, S., Ismail, A. F., Sulaeman, E., and Hasan, M. H., 2019, "Experimental Correlation for Flow-Boiling Heat Transfer in a Micro-Gap Evaporator With Internal Micro-Fins," J. Adv. Res. Fluid Mech. Therm. Sci., **54**, pp. 1–8.

[21] Alam, T., Lee, P. S., Yap, C. R., and Jin, L., 2013, "A Comparative Study of Flow Boiling Heat Transfer and Pressure Drop Characteristics in Microgap and Microchannel Heat Sink and An Evaluation of Microgap Heat Sink for Hotspot Mitigation," Int. J. Heat Mass Transfer, **58**(1–2), pp. 335–347.

[22] Majhi, M., Nayak, A. K., and Banerjee, A., 2020, "Enhanced Electro-Osmotic Flow of Power-Law Fluids in Hydrophilic Patterned Nanochannel," ASME J. Fluids Eng., **142**(10), p. 101201.

[23] Banerjee, A., Nayak, A. K., and Weigand, B., 2020, "A Comparative Analysis of Mixing Performance of Power-Law Fluid in Cylindrical Microchannels With Sudden Contraction/Expansion," ASME J. Fluids Eng., **142**(6), p. 061201.

[24] Gatski, T., and Grosch, C., 1985, "Embedded Cavity Drag in Steady Laminar Flow," AIAA J., **23**(7), pp. 1028–1037.

[25] Mohammadi, A., and Floryan, J. M., 2015, "Numerical Analysis of Laminar-Drag-Reducing Grooves," ASME J. Fluids Eng., **137**(4), p. 041201.

[26] Chai, L., Xia, G. D., and Wang, H. S., 2016, "Parametric Study on Thermal and Hydraulic Characteristics of Laminar Flow in Microchannel Heat Sink With Fan-Shaped Ribs on Sidewalls—Part 2: Pressure Drop," Int. J. Heat Mass Transfer, **97**, pp. 1081–1090.

[27] Lang, A. W., and Johnson, T. J., 2010, "Drag Reduction Over Embedded Cavities in Couette Flow," Mech. Res. Commun., **37**, pp. 432–435.

[28] Rawool, A. S., Mitra, S. K., and Kandlikar, S. G., 2006, "Numerical Simulation of Flow Through Microchannels With Designed Roughness," Microfluid. Nanofluid., **2**(3), pp. 215–221.

[29] Djenidi, L., Anselmet, F., Liandrat, J., and Fulachier, L., 1994, "Laminar Boundary Layer Over Riblets," Phys. Fluids, **6**(9), pp. 2993–2999.

[30] Daschiel, G., Peric, M., Jovanovic, J., and Delgado, A., 2013, "The Holy Grail of Microfluidics: Sub-Laminar Drag by Layout of Periodically Embedded Microgrooves," Microfluid. Nanofluid., **15**(5), pp. 675–687.

[31] Bixler, G. D., and Bhushan, B., 2013, "Bioinspired Micro/Nanostructured Surfaces for Oil Drag Reduction in Closed Channel Flow," Soft Matter, **9**(5), pp. 1620–1635.

[32] Wang, L., Wang, C., Wang, S., Sun, G., and You, B., 2021, “Design and Analysis of Micro-Nano Scale Nested-Grooved Surface Structure for Drag Reduction Based on ‘Vortex-Driven Design’,” Eur. J. Mech. B/Fluids, **85**, pp. 335–350.

[33] Ghaddar, N. K., Korczak, K. Z., Mikic, B. B., and Patera, A. T., 1986, “Numerical Investigation of Incompressible Flow in Grooved Channels. Part 1, Stability Self-Sustained Oscillations,” J. Fluid Mech., **163**, pp. 99–127.

[34] Asadzadeh, H., Moosavi, A., and Etemadi, A., 2019, “Numerical Simulation of Drag Reduction in Microgrooved Substrates Using Lattice-Boltzmann Method,” ASME J. Fluids Eng., **141**(7), p. 071111.

[35] Kharati-Koopaee, M., and Zare, M., 2015, “Effect of Aligned and Offset Roughness Patterns on the Fluid Flow and Heat Transfer Within Microchannels Consist of Sinusoidal Structured Roughness,” Int. J. Therm. Sci., **90**, pp. 9–23.

[36] Xu, F., Zhong, S., and Zhang, S., 2018, “Vortical structures and Development of Laminar Flow Over Convergent-Divergent Riblets,” Phys. Fluids, **30**(5), p. 051901.

[37] Guo, T., Zhong, S., and Craft, T., 2020, “Control of Laminar Flow Separation Over a Backward-Facing Rounded Ramp With C-D Riblets – The Effects of Riblet Height, Spacing and Yaw Angle,” Int. J. Heat Fluid Flow, **85**, p. 108629.

[38] Raayai-Ardakani, S., and McKinley, G. H., 2017, “Drag Reduction Using Wrinkled Surfaces in High Reynolds Number Laminar Boundary Layer Flows,” Phys. Fluids, **29**(9), p. 093605.

[39] Wang, Y., 2018, “Effects of Grooves on Drag in Laminar Channel Flow,” Electronic Thesis and Dissertation Repository, 5487, The University of Western Ontario, London, ON, Canada, accessed Feb. 2, 2023, https://ir.lib.uwo.ca/etd/5487